



HAL
open science

Time-lapse global inversion for surface-waves: A differential approach using a linear approximation of the Rayleigh wave phase velocity

A. Wang, Odile Abraham, Donatienne Leparoux

► To cite this version:

A. Wang, Odile Abraham, Donatienne Leparoux. Time-lapse global inversion for surface-waves: A differential approach using a linear approximation of the Rayleigh wave phase velocity. *Wave Motion*, 2023, 122, pp.103193. 10.1016/j.wavemoti.2023.103193 . hal-04187673

HAL Id: hal-04187673

<https://univ-eiffel.hal.science/hal-04187673>

Submitted on 25 Aug 2023

HAL is a multi-disciplinary open access archive for the deposit and dissemination of scientific research documents, whether they are published or not. The documents may come from teaching and research institutions in France or abroad, or from public or private research centers.

L'archive ouverte pluridisciplinaire **HAL**, est destinée au dépôt et à la diffusion de documents scientifiques de niveau recherche, publiés ou non, émanant des établissements d'enseignement et de recherche français ou étrangers, des laboratoires publics ou privés.

Time-lapse global inversion for surface-waves: a differential approach using a linear approximation of the Rayleigh wave phase velocity

A. Wang^a, O. Abraham^b, D. Leparoux^b

^a*Univ Rouen Normandie, UNICAEN, CNRS, M2C UMR 6143, F-76000, Rouen, France*

^b*Gustave Eiffel University, Campus Nantes, Allée des Ponts et Chaussées, Routes de Bouaye - CS 5004, 44344 Bouguenais, France*

Abstract

Surface-wave methods have a wide range of possible applications in the monitoring of near-surface media. In classical monitoring methods, data measured at different times are inverted separately and independently, and the difference in the inversion results reflects the temporal changes in the medium. However, the results obtained in this way can be affected by the reproducibility of experimental measurements, measurement and inversion uncertainties, etc. In this study, we introduce Differential Inversion in surface-wave methods, which uses the difference between measured data as inversion input data, instead of the measured data themselves. More precisely, a linear approximation of Rayleigh wave phase velocity associated with its sensitivity kernel is used to relate the data difference with the model variations. This differential inversion approach is firstly tested with numerical data generated in a series of two-layer models in order to estimate the limitations of the linear approximation with a global

Email addresses: ao.wang@univ-rouen.fr (A. Wang), odile.abraham@univ-eiffel.fr (O. Abraham), donatienne.leparoux@univ-eiffel.fr (D. Leparoux)

inversion approach. It is shown that when the shear-wave velocity variation is more than 5%, the linear assumption is no longer relevant. With respect to the 5% of variation, we apply the differential inversion approach on laboratory data, obtained from three reduced-scale epoxy-resin two-layer models. The results show the feasibility of the differential inversion to estimate the shear-wave velocity differences between epoxy-resin models. The short calculation time is one of its advantages. However, a good estimation on the baseline is required in order to calculate the sensitivity kernel. Finally, the robustness of the proposed approach is verified by numerical data, using the Spectral Element Method to simulate wave propagation in the presence of an under-surface cavity.

Keywords: Surface-wave methods, Differential inversion, Small scale models, Rayleigh wave sensitivity kernel, Spectral Element Method.

1 **1. Introduction**

2 Surface-wave (SW) methods are widely used in near-surface applications, be-
3 cause they allow the quantitative assessment of mechanical property parameters
4 without difficulties thanks to the use of lightweight sources. Indeed, while body
5 waves are highly attenuated in altered and unconsolidated underground environ-
6 ments, surface-waves remain very energetic and easy to record. For this reason,
7 SW methods are increasingly used for monitoring subsurface media which are
8 sensitive to environmental changes. For example, to monitor the water table
9 level in shallow aquifers (Pasquet et al., 2015), internal erosion in dams (Planès
10 et al., 2016), water penetration in dikes (Joubert et al., 2018), thaw-induced
11 subsidence in permafrost (Ajo-Franklin et al., 2017), and to estimate climatic

12 effects on railway embankments (Bergamo et al., 2016), water content and water
13 potential in the vadose zone under different weather and seasonal effects (Lu,
14 2014), etc.

15 The aim of time-lapse monitoring is to monitor temporal variations through
16 a series of measurements made at different times. Variations in the medium
17 can be estimated by comparing the observables of the measured data, such as
18 SW phase velocity (V_{ph}) variations. However, if quantitative estimations of the
19 parameter variations in the medium are needed, e.g., the temporal variations of
20 S-wave velocity (V_s) spatial mapping, an inversion process is essential. Quan-
21 titative SW imaging methods invert SW dispersion data, usually the phase or
22 group velocity, to obtain the mechanical properties of a medium via V_s as func-
23 tion of depth. For example, in order to estimate the climate effects on a railway
24 embankment, Bergamo et al. (2016) measured and inverted the Rayleigh wave
25 V_{ph} and attenuation curves to construct the time-lapse model of V_s . In this
26 study, a velocity variation of 10% was estimated quantitatively for the Rayleigh
27 wave and the inverted V_s . Ikeda et al. (2017) inverted surface-wave V_{ph} disper-
28 sion data to monitor the environmental influences on shallow seismic velocity
29 above the so called Aquistore CO_2 storage site. Higher V_{ph} values are observed
30 in winter due to the increase of V_s with a higher degree of frozen saturated rock.
31 More recently, Wang et al. (2020b) have studied the sensitivity of the Rayleigh
32 wave phase and group velocities with respect to the V_s . The authors showed
33 that these two types of dispersion data are not sensitive enough to small vari-
34 ations in the deep medium to accurately obtain good inversion results. They

35 then proposed to use the frequency derivative of the Rayleigh V_{ph} as inversion
36 input data to improve the recovery of small variations in the deep medium.

37 This lack of precision in inversion results is due to several key points in
38 the entire inversion methodology, including the sensitivity of the input data
39 to the inverted medium parameter as well as measurement uncertainty. This
40 uncertainty should be taken into account during signal processing as it impacts
41 the estimation of the variations in the medium for time-lapse monitoring. In
42 the case of surface-wave approaches, the probability of measurement error is
43 generally considered as a Gaussian distribution (Tarantola, 2005; Menke, 2018).
44 More precisely, O'Neill (2004) pointed out that a Lorentzian distribution is more
45 appropriate than a Gaussian distribution for low frequencies, and proposed to
46 use a realistic dispersion error to estimate data uncertainty. More recently,
47 Dangeard et al. (2018) proposed a processing workflow to estimate picking errors
48 during manual picking for extracting the surface-wave V_{ph} dispersion curve.

49 In view of the existing studies above, the idea of differential inversion gets our
50 attention, i.e., using the difference of data measured at different times (named
51 baseline and repeatline respectively) as the input data in the inversion process
52 and extracting model difference directly, instead of inverting two measured data
53 separately and independently and estimating the model variations from their
54 inversion result difference. Similar ideas have appeared in some researchers'
55 works, e.g., the Double Difference Full Waveform Inversion using the subtraction
56 of baseline and repeatline to remove the coherent noise and keep the difference
57 mainly caused by model parameter variations (Watanabe et al., 2004; Denli and

58 Huang, 2009; Asnaashari et al., 2012; Yang et al., 2015), or the application of
59 passive SW methods to extract V_{ph} relative variation through the cross-wavelet
60 transform and estimate the 1D V_s variation using a relation of the SW sensitivity
61 kernel (Mordret et al., 2020).

62 The methods mentioned above work on the seismic waveforms, which take
63 a long computing and processing time, therefore only a local optimization ap-
64 proach can be considered to infer the model variations. In this study, the pro-
65 posed differential inversion uses a linear approximation of the Rayleigh wave
66 V_{ph} , by applying its analytical formulation of sensitivity kernel to associates
67 model parameter variation with Rayleigh wave V_{ph} variation, making it possi-
68 ble to use the V_{ph} difference in the differential inversion process. This original
69 process will be conducted by a global optimization approach in the inversion
70 problem.

71 In the first section below, the methodology as well as numerical and experi-
72 mental tools used for the study are presented, i.e. the linear approximation of
73 Rayleigh wave V_{ph} , the optimization process for inversion, the laboratory mea-
74 surement bench and the applied numerical method for providing SW data. Then
75 the proposed differential inversion is introduced. Since the analytical formula-
76 tion of the sensitivity kernel is used, we abbreviate this approach as ADTLSWI
77 (Analytical Differential Time-Lapse Surface-Wave Inversion) hereinafter. The
78 behavior of ADTLSWI is studied numerically, using theoretical V_{ph} dispersion
79 curves in order to analyze the limits of the ADTLSWI under the condition of
80 large and small model parameter variations. Then, in the third section, the

81 robustness of ADTLSWI is verified using experimental data and numerical data
82 respectively. The former uses laboratory data measured on reduced-scale epoxy-
83 resin models to test if the proposed approach is able to estimate the variations in
84 the deep layer in a controlled environment; the later uses numerical data calcu-
85 lated by Spectral Element Method (Komatitsch and Vilotte, 1998; Komatitsch
86 and Tromp, 1999) to simulate the case of a perturbation of the under-surface
87 structure. The advantages and limits of ADTLSWI, that are studied here in a
88 global inversion framework, are also commented.

89 **2. Material and methods**

90 In this section, we present the material and methods used in this study. First,
91 the linear approximation of Rayleigh wave V_{ph} with respect to model parameters
92 is given. Then the experimental set-ups for the laboratory measurement are
93 described. The numerical method which is used for the synthetic data generation
94 is also introduced. In the end, the inversion technique which is applied for all
95 the inversion process mentioned in this study is presented.

96 *2.1. Linear approximation of Rayleigh wave phase velocity*

97 According to Taylor's theorem, the linear approximation of the Rayleigh
98 wave phase velocity $V_{ph}(\mathbf{m})$, which is a function of model parameters \mathbf{m} (in-
99 cluding S-wave velocity V_s , P-wave velocity V_p , density ρ and the layer thickness
100 h) can be written as

layer (i)	$V_{p_i}^{ref}$ [m/s]	$V_{s_i}^{ref}$ [m/s]	ρ_i^{ref} [kg/m ³]	ν_i^{ref}	h_i^{ref} [m]
1	1000	600	1500	0.22	8.0
2	2000	1100	2200	0.28	∞

Table 1: Parameters of a two-layer reference model. V_p : compressional-wave velocity; V_s : shear-wave velocity; ρ : density; ν : Poisson’s ratio; and h : layer thickness.

$$V_{ph}(\mathbf{m}) = V_{ph}(\mathbf{m}_b) + \left[\frac{dV_{ph}}{d\mathbf{m}} \right]_{\mathbf{m}_b} (\mathbf{m} - \mathbf{m}_b) + o[(\mathbf{m} - \mathbf{m}_b)], \quad (1)$$

101 with $\lim_{\mathbf{m} \rightarrow \mathbf{m}_b} o[(\mathbf{m} - \mathbf{m}_b)] = 0$ and \mathbf{m}_b representing the baseline model pa-
102 rameters. $\left[\frac{\partial V_{ph}}{\partial m} \right]$ is the sensitivity kernel of Rayleigh wave V_{ph} with respect
103 to model parameters \mathbf{m} . The calculation of sensitivity kernel can be found in
104 numerous literature, e.g. Takeuchi et al. (1972); Wang et al. (2020b). The au-
105 thor mentioned that only the first order of partial derivative of Rayleigh wave
106 V_{ph} with respect to \mathbf{m} can be calculated analytically Aki and Richards (2002).
107 Therefore, higher orders are not considered in this study by neglecting the term
108 $o[(\mathbf{m} - \mathbf{m}_b)]$. Writing the derivative of V_{ph} in Eq. 1 as the sum of partial
109 derivatives for each model parameter, we obtain:

$$V_{ph}(\mathbf{m}) \approx V_{ph}(\mathbf{m}_b) + \sum_{m_i} \left[\frac{\partial V_{ph}}{\partial m_i} \right]_{m_{i_b}} (m_i - m_{i_b}), \quad (2)$$

110 with $i \in [1, 4]$ and $m_i = (V_s, V_p, \rho, h)$.

111 Studies such as Dziewonski and Anderson (1981); Wang et al. (2020b) have
112 shown that V_s has more effect on Rayleigh wave V_{ph} compared to V_p and ρ .
113 Figures in Appendix A show that for a two-layer model as in Tabke 1, V_{ph} is

114 7 times more sensitive to V_s than to V_p and ρ for the deep layer. Considering
 115 this behavior, this study will be carried out under the assumption that only V_s
 116 changes, whereas V_p and ρ remain with the same values. The V_s variation ratio
 117 is defined as:

$$\alpha(V_{s_j}, b, r) = \frac{V_{s_j}^r - V_{s_j}^b}{V_{s_j}^b} \quad (3)$$

118 where $V_{s_j}^b$ and $V_{s_j}^r$ are the S-wave velocity of the j th layer for the baseline \mathbf{m}_b
 119 and the repeatline \mathbf{m}_r respectively.

120 2.2. Laboratory data

121 Laboratory data are used to test the feasibility of the proposed approach in
 122 a controlled context. Three reduced-scale epoxy-resin models, named $C25$, $C45$
 123 and $C65$, respectively, have been designed in order to simulate small variations in
 124 the medium to mimic time-varying models at three different times. The model
 125 parameters and the dimensions of the $C25$ model are presented in Table 2.
 126 Fig. 1 (a) presents the $C25$ model and the experimental set-up: the edges of all
 127 the models are rounded according to arcs of circles in order to minimize and
 128 delay the boundary effects (Pageot et al., 2015). The radius of the rounded edges
 129 must be larger than or equal to the central wavelength, which is 12 mm for all
 130 three epoxy-resin models used in this study. $C45$ and $C65$ have the same shape
 131 as $C25$, but have different V_s in their deep layer: 1100 m/s for $C45$ and 1160 m/s
 132 for $C65$. The variations of the V_s in the deep layer are $\alpha(V_{s_2}, C25, C45) = 1.8\%$
 133 and $\alpha(V_{s_2}, C45, C65) = 5.4\%$, calculated using Eq. 3.

layer	V_{p_i} [m/s]	V_{s_i} [m/s]	ρ_i [kg/m ³]	ν_i	h_i [mm]	l [mm]	w [mm]
1	1300	708	450	0.29	7.2	265	235
2	2048	1080	1300	0.37	203	265	235

Table 2: C25 model parameters and dimensions. h_i : layer thickness; l and w : length and width of model. The scale ratio between the numerical and the experimental model dimensions is 1000 (Pageot et al., 2017).

134 The measurements of the three epoxy-resin models were carried out at the
135 MUSC¹ laboratory (Bretaudeau et al., 2011; Valensi et al., 2015; Pageot et al.,
136 2017). Non-Contact Ultrasonic Measurement allows reproducing the same con-
137 figuration as in field measurements but in a controlled environment on reduced-
138 scale models. To do this, a scale ratio in time and distance is assumed (1000
139 in this work) and ultrasonic sensors are used. A piezo-electric transducer is
140 used as an active source to generate a Ricker wavelet with a center frequency
141 of 100 kHz. A moving laser interferometer measures the particle displacement,
142 with a sampling rate equal to 10 MHz. Fig. 1 (b) gives information about the
143 positions of the source and receivers. The distance between the source and the
144 first receiver is 12 mm and the receivers are lined up for a total length equal to
145 90 mm with a spacing between receivers equal to 1 mm.

146 In Fig. 2, the measured seismograms are superimposed in order to see the
147 differences between the three data-sets. Fig. 3 presents the measured Rayleigh
148 wave dispersion diagrams of the epoxy-resin models using the phase-difference

¹Mesure Ultrasonore Sans-Contact, or Non-Contact Ultrasonic Measurement in English

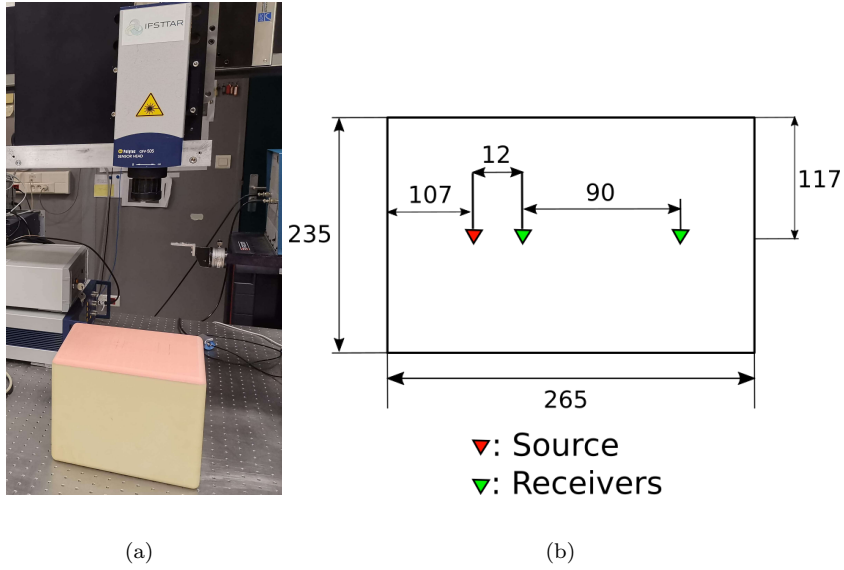
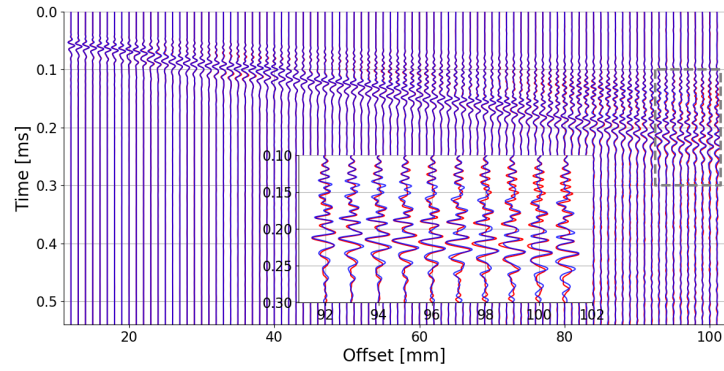


Figure 1: (a) Experimental set-up and the two-layer resin model. (b) Position of source and the receiver vector for the epoxy-resin model measurement.

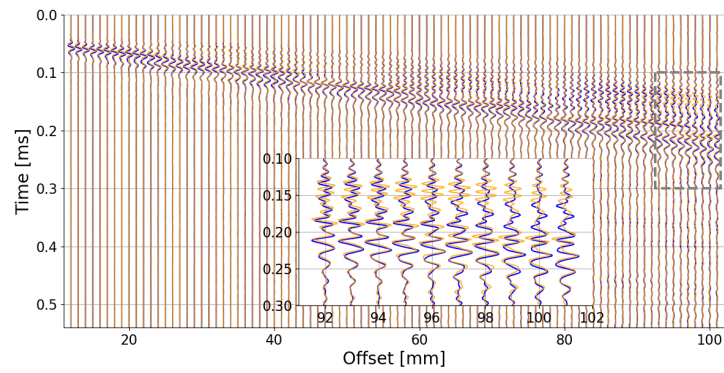
149 processing method (Mokhtar et al., 1988; Park et al., 1998) with V_{ph} dispersion
 150 curves in black dots.

151 2.3. Numerical validation by Spectral Element Method

152 The Spectral Element Method (SEM) is used to generate data to analyze
 153 the robustness of the method. The goal is to provide altered but controlled
 154 data to test the effectiveness of the ADTLSWI process. As shown by Gélis
 155 et al. (2005), the presence of a cavity alters the assessed dispersion diagram and
 156 the associated dispersion curve of SW. This configuration is therefore used to
 157 simulate a non perfect two-layer model by including this perturbation (supposed
 158 to be unknown) to the under-surface structure without seeking to reconstruct it.
 159 The numerical model is based on the two-layer model used in the experimental

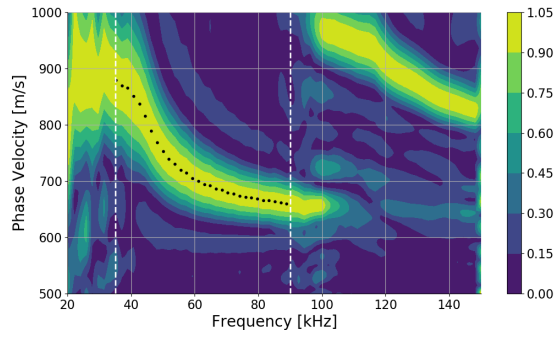


(a)

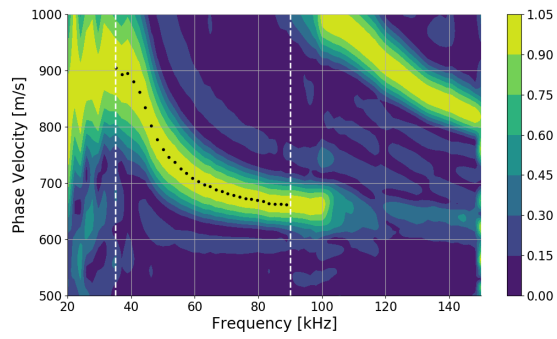


(b)

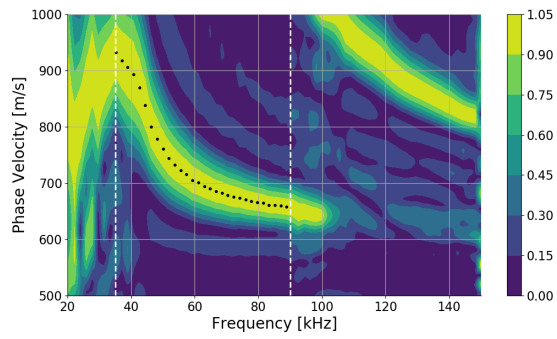
Figure 2: Measured seismograms for resin models. Red: $C25$; blue: $C45$; orange: $C65$. Signals in the grey rectangles ($t \in [0.1, 0.3]$ ms, $x \in [92, 101]$ mm) are zoomed for clearer visualization.



(a)



(b)



(c)

Figure 3: Measured dispersion diagrams of epoxy-resin models (a) *C25*, (b) *C45* and (c) *C65*. Black dots: the Rayleigh wave phase velocity. White dashed line: the frequency range used in the inversion process.

160 test, with a rectangular cavity situated under-surface. In this case, the direct
161 problem still using a two-layer model in SW dispersion curve calculation is
162 erroneous. The robustness of ADTLSWI is tested under this situation.

163 The baseline model uses parameters in Table 2, with a $40\text{ mm} \times 20\text{ mm}$ rect-
164 angular cavity placed 5 mm beneath the interface. In this numerical test, a free
165 software SPECFEM2D ² is used to simulate full-wave propagation (Komatitsch
166 and Vilotte, 1998; Komatitsch and Tromp, 1999). In order to test the stability
167 of the numerical model and the effect of cavity, a two-layer model without cav-
168 ity is firstly calculated and the results are compared with the baseline model
169 in the presence of cavity. With model parameters in Table 2, the maximum
170 wavelength is around 22 mm ($V_{ph} \approx 900\text{ m/s}$ at $f = 40\text{ kHz}$) which is in the
171 same order of magnitude as the cavity dimension. Fig. 4 shows the difference
172 between the dispersion curves of the numerical two-layer model, with and with-
173 out the cavity, especially around 50 kHz where the dispersion curve is altered
174 in case of the cavity presence. It should be point out that systematic study of
175 the effects of the cavity size with respect to the wavelength, the location of the
176 cavity, the measurement set-ups and the interface, is beyond the scope of this
177 study. Details of SPECFEM settings, model geometry and mesh generation, as
178 well as extracted seismograms, dispersion diagrams and dispersion curves are
179 available in Appendix B. The numerical data shows that in a two-layer model
180 with parameters in Table 2, the energy is dominated by the fundamental mode.

²<https://github.com/SPECFEM>

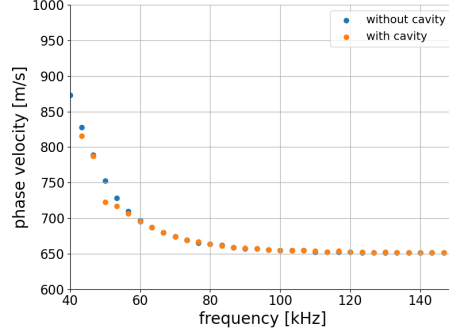


Figure 4: Dispersion curves of numerical models (a) without cavity and (b) with cavity.

181 Therefore, only the fundamental mode of the Rayleigh wave phase velocity is
 182 considered in the following of this study.

183 *2.4. Inversion algorithm*

A global optimization algorithm, the Neighborhood Algorithm (NA), is used for this study. Proposed by Sambridge (1999b,a) and the improved by Wathelet (2008), the NA uses Voronoi cells to sample the parameter space and generate models in a pseudo-random way. In the NA inversion, the objective function calculates the $L2$ norm between the two phase velocity differences (Wathelet, 2004):

$$misfit(\Delta \mathbf{V}_{\text{ph}}, \Delta \mathbf{V}'_{\text{ph}}) = \sqrt{\frac{1}{N_f} \sum_{N_f} (\Delta V_{ph} - \Delta V'_{ph})^2}. \quad (4)$$

In order to have the objective function in the range $[0, 1]$, the exponential of the misfit value is used by calculating the indicator P :

$$P = \exp(-misfit) \quad (5)$$

184 In this way, the proposed differential inversion uses NA where a sensitiv-

185 ity kernel relates the variation of measured data to the change of the model
 186 parameters. In the following section, the workflow of proposed differential in-
 187 version, ADTLSWI, is presented, as well as the limitations of this approach with
 188 different variation ratio of V_s in the model.

189 **3. Analytical Differential Time-Lapse Surface-Wave Inversion (ADTL-** 190 **SWI)**

191 *3.1. Workflow of ADTLSWI*

192 Based on the linear approximation of the Rayleigh wave V_{ph} in Eq. 2, we pro-
 193 pose a new time-lapse inversion, using the difference of the V_{ph} as the inversion
 194 input data. Fig. 5 shows the work-flow of this time-lapse inversion.

195 $\mathbf{V}_{\mathbf{ph}}^b$ and $\mathbf{V}_{\mathbf{ph}}^r$ are two measured phase velocities in a time-varying medium
 196 at different times, with b and r referring respectively the *baseline* and the *re-*
 197 *peatline*. Assuming the initial state of the medium (the baseline model \mathbf{m}_b) is
 198 known, the inversion process searches the new state of the medium (the repeat-
 199 line model \mathbf{m}_r) after some unknown variations have occurred in the medium.

200 $\Delta\mathbf{V}_{\mathbf{ph}}$ calculates the simple difference between the two measured phase veloc-
 201 ities: $\Delta\mathbf{V}_{\mathbf{ph}} = \mathbf{V}_{\mathbf{ph}}^r - \mathbf{V}_{\mathbf{ph}}^b$. Based on the baseline model parameter \mathbf{m}_b , the
 202 sensitivity kernel of the baseline $\left[\frac{\partial\mathbf{V}_{\mathbf{ph}}}{\partial\mathbf{m}}\right]_{\mathbf{m}_b}$ can be calculated.

203 The modification of the model parameter ($\Delta\mathbf{m}$) is the unknown in the inver-
 204 sion process. For that, the model difference $\Delta\mathbf{m}$ is calculated through the simple
 205 difference: $\Delta\mathbf{m} = \mathbf{m}_r - \mathbf{m}_b$, where \mathbf{m}_r is tested for several values searched in
 206 the parameter space in the NA. Using the linear approximation of the Rayleigh

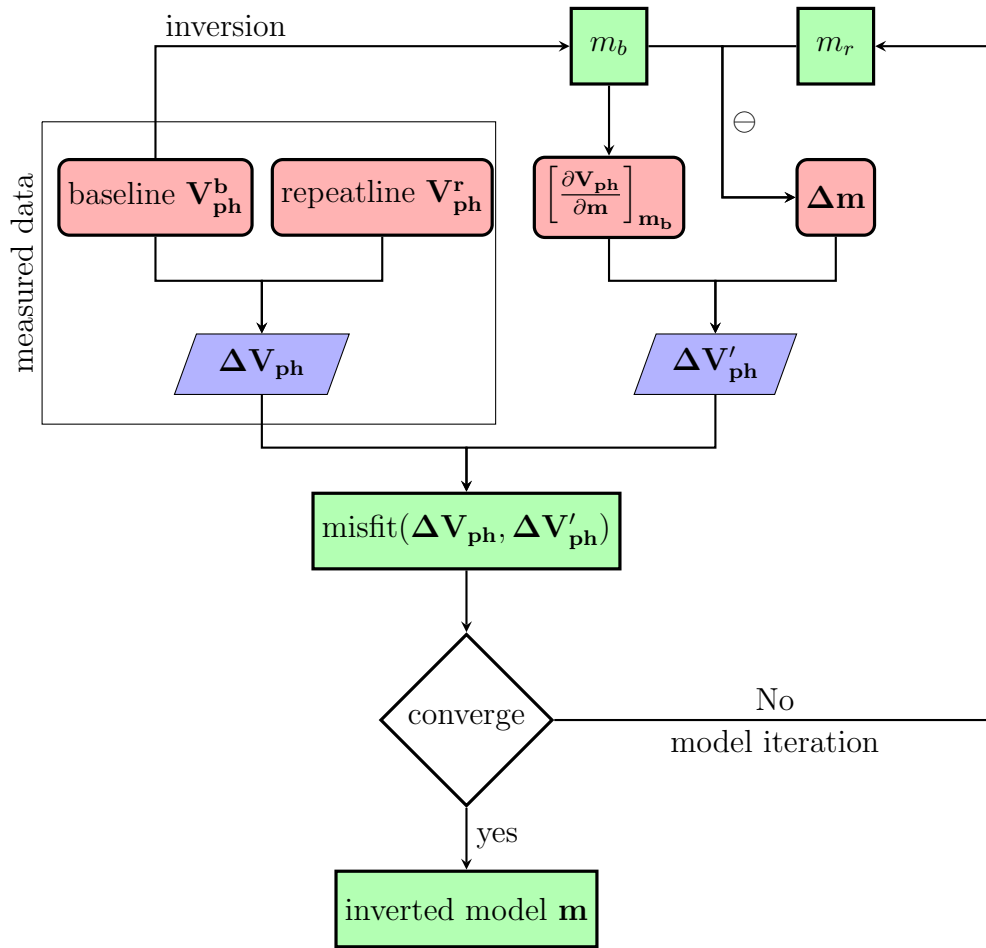


Figure 5: Work-flow of ADTLSWI. \mathbf{m}_b is recovered by a previous inversion of the baseline measurement \mathbf{b} ; \mathbf{r} is the new model tested, as defined by the NA depending on the misfit values of the previous iteration.

207 wave V_{ph} in Eq. 1, the phase velocity difference $\Delta \mathbf{V}'_{ph}$ can be calculated:

$$\Delta \mathbf{V}'_{ph} = \sum_{m_i} \left[\frac{\partial V_{ph}}{\partial m_i} \right]_{m_{i_b}} \Delta \mathbf{m}_i. \quad (6)$$

208 Note that the ADTLSWI uses a global optimization technique (NA) which
 209 does not depend on any initial model. However, since the ADTLSWI uses $\Delta \mathbf{V}_{ph}$
 210 as inversion input data under the linear assumption of the Rayleigh wave V_{ph} ,
 211 when the variation is too great, the linear assumption is no longer valid. In the
 212 following, we test this method using the numerical dispersion data to assess the
 213 feasibility and the limits of this method. The first test uses a series of models
 214 with large V_s variations ($\alpha(V_s) \in 16\%$) in order to test the limitation of the
 215 ADTLSWI approach. The second test has smaller v_s variations ($\alpha(V_s) \in 5\%$)
 216 and the inversion results are compared with other SW inversion approaches.

217 3.2. Error estimation

218 A two-layer model, named baseline \mathbf{m}_b , is used as the reference model. Its
 219 sensitivity kernel is calculated with respect to V_s . The model parameters of the
 220 baseline are described in Table 1. A series of models, named repeatline \mathbf{m}_r , are
 221 similar to the baseline parameters except for the S-wave velocities which are
 222 modified for each \mathbf{m}_r model.

223 Eq. 1 can be used to estimate the phase velocity of a repeatline model \mathbf{m}_r
 224 from knowledge of the phase velocity of a baseline model \mathbf{m}_b , under the condi-
 225 tion that models \mathbf{m}_b and \mathbf{m} are close enough for the variations between $V_{ph}(\mathbf{m})$
 226 and $V_{ph}(\mathbf{m}_b)$ to be considered linear. In order to analyze the limits of Eq. 1

227 validity, the phase velocity estimated using Eq. 1 will be compared with its the-
 228 oretical value. The S-wave velocity variation ratio is defined as in Eq. 3. In the
 229 following study, the S-wave velocity variation ratio of the repeatline for both
 230 layers are limited to the range: $\alpha(V_{s_1}) \in [-15, +15]\%$, $\alpha(V_{s_2}) \in [-15, +15]\%$.

231 The dispersion curves of the baseline and the repeatline (calculated using
 232 the Geopsy software (Wathelet, 2004)) are named $V_{ph}(\mathbf{m}_b)$ (abbreviated as V_{ph}^b)
 233 and $V_{ph}(\mathbf{m}_r)$ (abbreviated as V_{ph}^r) respectively. Using Eq. 2, the phase velocity
 234 of the repeatline can be estimated:

$$V_{ph}^{est}(\mathbf{m}_r) = V_{ph}(\mathbf{m}_b) + \sum_{m_i^r} \left[\frac{\partial V_{ph}}{\partial m_i} \right]_{m_i^b} (m_i^r - m_i^b). \quad (7)$$

235 The error between the estimated and theoretical phase velocities (also called
 236 phase velocity error) of the repeatline is defined using the $L2$ norm:

$$err(V_{ph}(\mathbf{m}_r), V_{ph}^{est}(\mathbf{m}_r)) = \sqrt{\frac{1}{N_f} \sum_{N_f} \left(\frac{V_{ph}(\mathbf{m}_r) - V_{ph}^{est}(\mathbf{m}_r)}{V_{ph}(\mathbf{m}_r)} \right)^2} \times 100\% \quad (8)$$

237 with N_f being the number of frequencies sampled for the phase velocity disper-
 238 sion curve.

239 Fig. 6 shows the errors between the estimated and calculated dispersion
 240 curves of the repeatline, with the S-wave velocity variation ratio less than 15%.
 241 The phase velocity errors are greater for V_{s_1} than for V_{s_2} . Indeed, the Rayleigh
 242 wave phase velocity is more sensitive to the variations of the shallow medium
 243 (see section 2.1: Sensitivity Kernels). Thus, when the variation occurs in the
 244 shallow layer, it is more difficult to estimate the correct phase velocity using

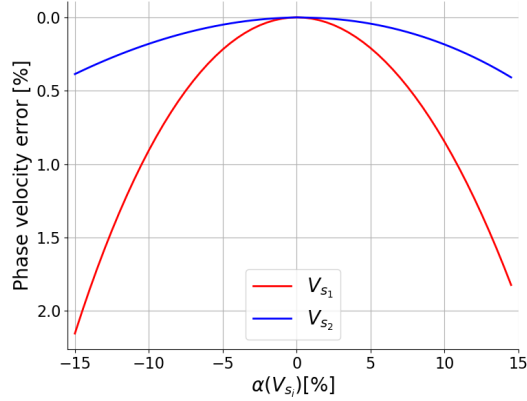


Figure 6: Phase velocity errors between the estimated and theoretical phase velocities of the repeatline. The variation ratios of both S-wave velocities are less than 15%.

245 Eq. 1. In other words, in the case of the shallow layer, we quickly move away
 246 from the hypothesis of linearity when the variation in S-wave velocity increases.

247 3.3. ADTLSWI with large S-wave velocity variations

248 The baseline model is the same as in Table 1 and the variation ratio of
 249 the repeatline models, described by Eq. 3, is such that $\alpha(V_{s_i}) \in [-16, +16]\%$
 250 (the variation ratio $\alpha(V_{s_i}, b, r)$ is simplified as $\alpha(V_{s_i})$ in the following). Three
 251 inversion tests are performed: (1) $\alpha(V_{s_1}) \in [-16, 16]\%$, $\alpha(V_{s_2}) = 0$; (2) $\alpha(V_{s_1}) =$
 252 0 , $\alpha(V_{s_2}) \in [-16, 16]\%$; (c) $\alpha(V_{s_1}) = \alpha(V_{s_2}) \in [-16, 16]\%$. Each test has 33
 253 repeatline models. Each repeatline model will be paired with the baseline model
 254 for the time-lapse inversion, thus 33×3 inversion results are analyzed.

255 For each inversion process, V_{ph}^b and V_{ph}^r are calculated theoretically using
 256 the Geopsy software (Wathelet, 2004) in the frequency range $[10, 150] Hz$ with
 257 a step of $0.5 Hz$. It should be pointed out that since the difference of the

258 phase velocity is the inversion input data, the parameter space is the range of
 259 variation between the baseline and the repeatline model parameters. Here in
 260 each inversion, the repeatline S-wave velocities V_{s_i} will be searched in the range
 261 $V_{s_i} \in [-20, +20]\% \times \Delta V_{s_i}$, where $\Delta V_{s_i} = V_{s_i}^r - V_{s_i}^b$. Other parameters (V_p , ρ
 262 and h_1) are fixed: their values are given in Table 1.

263 Among a total number of 1020 searched models for each inversion case, only
 264 those models whose objective function (defined in Eq. 5) has a value greater
 265 than 99% of the values associated with the best models will be selected: $P_i \geq$
 266 $99\% \times \max(P_i)$ with $i \in [1, 1020]$. The inversion results of the three inversion
 267 tests are presented in Fig. 7. Each group of colored dots corresponds to the
 268 results of one ADTLSWI with a pair of baseline-repeatline models and from
 269 blue to red, $\alpha(V_{s_i})$ decreases. This choice aims to visually differentiate the
 270 different zones of alpha values in the results. The black dot is the center of this
 271 group of inversion models. The gray triangle is the true position of $\alpha(V_{s_i})$ for
 272 each repeatline.

273 In Fig. 7 (a), the inversion results are presented as a function of the variation
 274 ratio $\alpha(V_{s_1}) \in [-16, 16]\%$ in the x-axis. In the y-axis, the inversion results are
 275 presented as the quotient of the difference between V_{s_2} and $V_{s_2}^b$ with respect to
 276 $V_{s_2}^b$ (noted as $\Delta V_{s_2}/V_{s_2}^b$). Since $\alpha(V_{s_2}) = 0$ in these inversions, the centers of the
 277 inversion results should form a line at $\Delta V_{s_2}/V_{s_2}^b = 0$. However, in Fig. 7 (a), the
 278 centers of the inversion results (black dots) have a parabolic shape: the inverted
 279 V_{s_2} is biased. In addition, the distances between the black dots and the grey
 280 dots become significant when $\alpha(V_{s_1}) > 5\%$. The result shows that when large

281 variations occur in V_{s_1} , the phase velocity cannot be correctly estimated due
 282 to the limits of linear approximation. The inversion results are thus biased not
 283 only for V_{s_1} but also for V_{s_2} .

284 In Fig. 7 (b), the inversion results are presented as a function of the variation
 285 ratio $\alpha(V_{s_2}) \in [-16, 16]\%$ in the x-axis, and as a function of $\Delta V_{s_1}/V_{s_1}^b$ in the
 286 y-axis. The inversion results of V_{s_1} are less biased compared to the inverted V_{s_2}
 287 in Fig. 7 (a). This corresponds to the error estimation in section 3.2: the high
 288 sensitivity of the Rayleigh wave V_{ph} with respect to V_{s_1} makes it more difficult
 289 to hold the linear approximation in Eq. 1. Consequently, the inversion results
 290 are more biased when variations occur at shallow depth.

291 In Fig. 7 (c), the variation ratios are equal for both layers, $\alpha(V_{s_1}) = \alpha(V_{s_2})$,
 292 so that the centers of the inversion results should line up (the grey dots). This
 293 is the case when $\alpha(V_{s_i}) \leq 5\%$. When $\alpha(V_{s_i}) = 5\%$, the inverted results of V_s
 294 are $\alpha(V_{s_1}) = 4.79\%$, $\alpha(V_{s_2}) = 4.56\%$ instead of 5%; when $\alpha(V_{s_i}) = -5\%$, the
 295 inverted results of V_s are $\alpha(V_{s_1}) = -5.17\%$, $\alpha(V_{s_2}) = -5.46\%$ instead of -5% .
 296 This means that when the same proportion of variation occurs in V_{s_1} and V_{s_2} ,
 297 it is more difficult to estimate the deep layer variation using the ADTLSWI,
 298 which corresponds to the low sensitivity of Rayleigh wave V_{ph} with respect to
 299 V_{s_2} .

300 These tests show the limit of the linear approximation for differential inver-
 301 sion in the context of a two-layer medium with model parameters in Table 1.
 302 According to these results, the ADTLSWI should be limited to cases where the
 303 model variations are lower than 5% for both layers, the value above which the

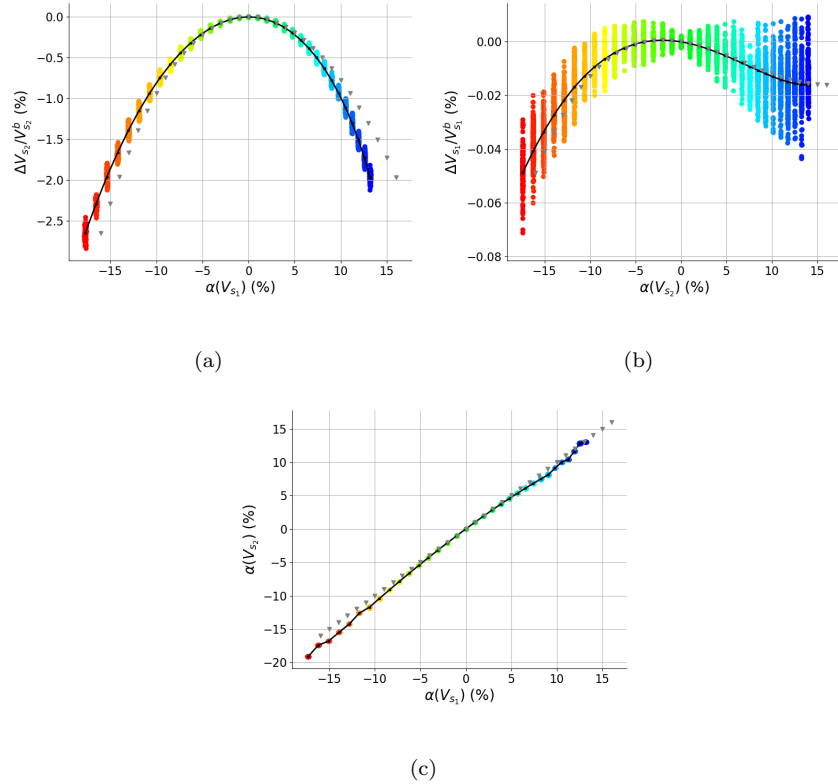


Figure 7: Inversion results using the ADTLSWI. Each group of colored dots corresponds to the selected models in this inversion: $\alpha(V_{s_i})$ decreases from blue to red. Black dots: the center of each inversion models. Grey triangle: the expected results of $\alpha(V_{s_i})$. (a) $\alpha(V_{s_1}) \in [-16, 16]\%$, $\alpha(V_{s_2}) = 0$. (b) $\alpha(V_{s_1}) = 0$, $\alpha(V_{s_2}) \in [-16, 16]\%$. (c) $\alpha(V_{s_1}) = \alpha(V_{s_2}) \in [-16, 16]\%$.

304 linear assumption is no longer relevant. Indeed, if the variation is less than
 305 5%, the mean of the family of results extracted for misfit values greater than
 306 99% compared to the maximum misfit value, reaches the correct expected value
 307 of the repeatline. In the next section, the ADTLSWI will be compared with
 308 other surface-wave inversion methods in the case of model parameter variations
 309 smaller than 5%.

310 *3.4. ADTLSWI with weak S-wave velocity variations*

311 For the two-layer model in Table 1, it has been shown that the ADTLSWI is
312 applicable if the S-wave velocity variation is less than 5%. Conforming to this
313 limit, the ADTLSWI will be applied to the same baseline and repeatline models
314 as before, using the theoretical phase velocities, and the inversion results will
315 be compared to other surface-wave inversion methods: the Rayleigh wave phase
316 velocity inversion (abbreviated as V_{ph} -SWI) and the frequency derivative of the
317 Rayleigh wave V_{ph} inversion (abbreviated as PVD-SWI) (Wang et al., 2020b).
318 The V_{ph} -SWI uses the theoretical V_{ph} dispersion curve as the inversion input
319 data. The PVD-SWI uses the combined data of the V_{ph} at high frequencies and
320 the frequency derivative of V_{ph} at low frequencies. The study of Wang et al.
321 (2020b) showed that the phase velocity derivative has a higher sensitivity to the
322 medium variation than the V_{ph} for the deep layer, so that a mixed approach
323 that combines the two types of input data lead to a robust inversion.

324 The three inversion input data are calculated theoretically in the frequency
325 range $[10, 150] Hz$ with a step of $0.5 Hz$. The combined data consists of the
326 phase velocity derivative when $f \leq 60 Hz$ and the phase velocity derivative
327 when $f > 60 Hz$. Since the variations between the baseline and the repeatline
328 models are small ($\alpha(V_{s_i}) \leq 5\%$), the model parameters are searched in the same
329 range for all the inversions: $V_{s_1} \in [560, 640] m/s$, $V_{s_2} \in [1040, 1160] m/s$, i.e.
330 $\Delta V_{s_1} \in [-40, 40] m/s$, $\Delta V_{s_2} \in [-60, 60] m/s$. All the other model parameters
331 are fixed and their values available in Table 1.

332 A total number of 1020 models are searched for each inversion and only

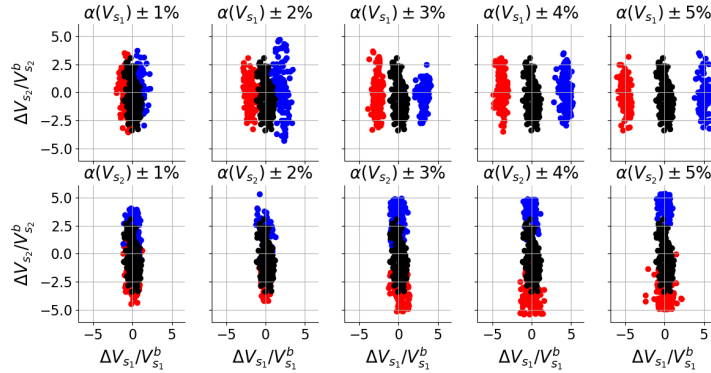


Figure 8: The inversion results of V_{ph} -SWI. Each dot corresponds to one inverted model with the colors representing the variation ratio of the medium. Red: $\alpha(V_{s_i}) < 0$; black: $\alpha(V_{s_i}) = 0$; blue: $\alpha(V_{s_i}) > 0$.

333 those models whose objective function (Eq. 5) has a value greater than 99% of
 334 the value associated with the best model are selected: $P_i \geq 99\% \times \max(P_i)$
 335 with $i \in [1, 1020]$. In Fig. 8 and Fig. 9, the inversion results are presented as a
 336 function of V_{s_i} , normalized by the corresponding values of the baseline model
 337 (Table 1).

338 As predicted in Wang et al. (2020b), V_{ph} -SWI is not capable of estimating
 339 weak variations of the medium, especially for the deep layer (Fig. 8). When
 340 $\alpha(V_{s_1}) \leq 2\%$ and $\alpha(V_{s_2}) \leq 5\%$, the inversion results are superimposed. The
 341 inversion results of the PVD-SWI can be separated when the variation is larger
 342 than 2% for both layers (Fig. 9). Therefore, the PVD-SWI method can estimate
 343 weak variations of the medium better than the V_{ph} -SWI approach, thanks to its
 344 higher sensitivity to the variation of the medium.

345 The inversion results of ADTLSWI in Fig. 10, which takes advantage of
 346 time-lapse measurements through the workflow presented in Fig. 5, show the

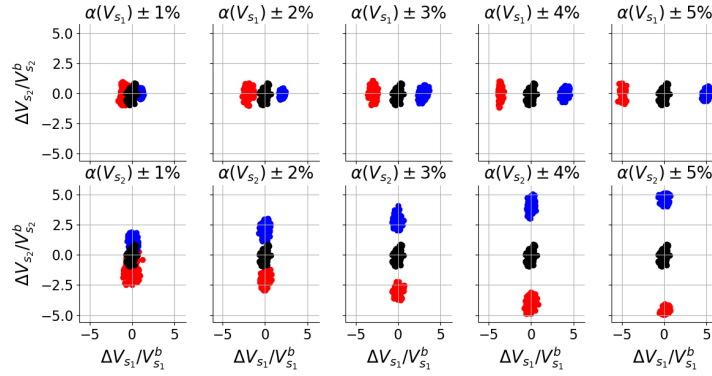


Figure 9: The inversion results of PVD-SWI. Each dot corresponds to one inverted model with the colors representing the variation ratio of the medium. Red: $\alpha(V_{s_i}) < 0$; black: $\alpha(V_{s_i}) = 0$; blue: $\alpha(V_{s_i}) > 0$.

347 best behavior. Indeed, the inversion results of each group are centered and
 348 there is no overlapping of the inversion results, even for the smallest variation
 349 ($\alpha(V_{s_i}) = 1\%$). However, a small bias for the centers of the inversion results can
 350 be observed when $\alpha(V_{s_1}) = 5\%$, which corresponds to the limits of the linear
 351 approximation of the Rayleigh phase velocity described previously. Another
 352 advantage of the ADTLSWI is its short computing time due to the fact that the
 353 forward problem is calculated only once for the sensitivity kernel of the baseline
 354 $\left[\frac{\partial \mathbf{V}_{ph}}{\partial \mathbf{m}} \right]_{\mathbf{m}_b}$ (Fig. 5). In other two surface-wave inversion methods, the forward
 355 problem is calculated for each searched model, which is the most computer
 356 time-consuming part of the algorithm.

357 Theoretical Rayleigh wave phase velocities have been used to analyze the
 358 ability of ADTLSWI for the estimation of weak variations of the medium. The
 359 use of ADTLSWI is valid when the variation of the medium is lower than 5%.
 360 The comparison of ADTLSWI with V_{ph} -SWI and the PVD-SWI shows that

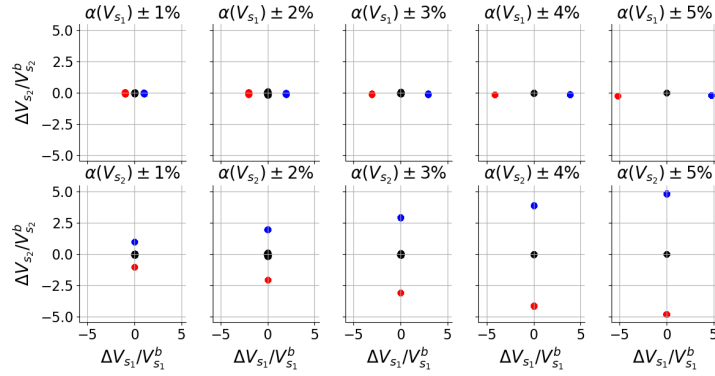


Figure 10: The inversion results of ADTLSWI. Each dot corresponds to one inverted model with the colors representing the variation ratio of the medium. Red: $\alpha(V_{s_i}) < 0$; black: $\alpha(V_{s_i}) = 0$; blue: $\alpha(V_{s_i}) > 0$.

361 ADTLSWI has the best behavior. In the next section, ADTLSWI will be applied
 362 to laboratory experimental data and numerical data, in order to confirm this
 363 result and test the robustness of the ADTLSWI approach.

364 4. Experimental validation and robustness test

365 4.1. Inversion of laboratory data

366 Two groups of ADTLSWI are tested in this section to recover material prop-
 367 erty variations thanks to couples of measured seismograms. First, the *C25* model
 368 is used as the baseline and *C45* as the repeatline, named *C25/C45*. Then, mod-
 369 els *C45* and *C65* are used as the baseline and the repeatline, named *C45/C65*.
 370 Both groups will share the following settings:

- 371 • h_1 is fixed (value available in Table 2);
- 372 • $\Delta V_{p_1} \in [-65, +65] m/s$, $\Delta V_{p_2} \in [-102, +102] m/s$;

- 373 • $\Delta\rho_1 \in [-22.5, +22.5] \text{ kg/m}^3$, $\Delta\rho_2 \in [-65, +65] \text{ kg/m}^3$;
- 374 • $\Delta V_{s_1} \in [-30, +30] \text{ m/s}$, $\Delta V_{s_2} \in [-10, 110] \text{ m/s}$;
- 375 • frequency range: $f \in [35, 90] \text{ kHz}$.

376 Because the V_{s_2} variation ratios are $\alpha(V_{s_2}, C25, C45) = 1.8\%$ and $\alpha(V_{s_2}, C45, C65) =$
377 5.4% , respectively, we search ΔV_{s_2} in the range $[-10, 110] \text{ m/s}$ which corre-
378 sponds to a variation range $[-0.9, 10]\%$. The parameter space for the rest of the
379 parameters, i.e. V_{s_1} , ρ_i , and V_{p_i} ($i = 1, 2$), are determined by $\alpha(m, \mathbf{b}, \mathbf{r}) \approx \pm 5\%$
380 for both inversions. The frequency limits are 35 kHz at low frequencies, be-
381 cause of a low signal-to-noise ratio, and 90 kHz at high frequencies in order to
382 extract only the fundamental model and to avoid higher mode perturbations for
383 all three models.

384 A total number of 27100 models are searched. The convergence curves (i.e.
385 the indicator P in Eq. 5) as a function of the iteration number are presented
386 in Fig. 11 for these tests. It can be seen that both inversion processes converge
387 ($P/P_{max} \approx 1$) when the iteration number is around 15000. The inverted mod-
388 els exceeding the black dashed line ($P \geq 99\% \times P_{max}$) are selected. More than
389 16000 models are selected for $C25/C45$ inversion and 13000 models for $C45/C65$
390 inversion. Table 3 compares the inverted results of V_s with the real values. The
391 mean values and the standard deviations of selected models are calculated for
392 both inversions. The mean value of the inverted ΔV_{s_1} for $C45/C65$ inver-
393 sion ($\Delta V_{s_1}^{inv} = -3.4 \text{ m/s}$) is 17 times greater than that of $C25/C45$ inversion
394 ($\Delta V_{s_1}^{inv} = -0.2 \text{ m/s}$), and the standard deviation 1.5 times higher. For $\Delta V_{s_2}^{inv}$,

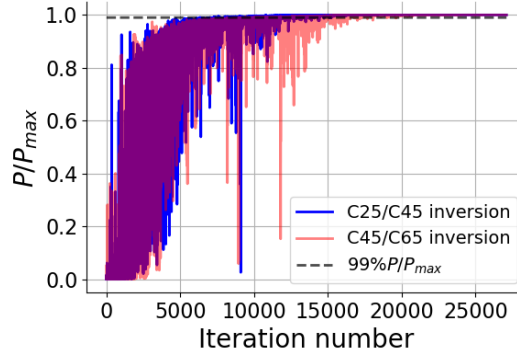


Figure 11: Convergence curves for ADTLSWI, using $C45$ and $C65$ as repeatline respectively.

395 the inverted result of $C25/C45$ has 1.2 m/s (+6%) of error, and $C45/C65$ has
 396 -5.7 m/s (-9.5%) of error which is 1.6 times higher than $C25/C45$.

397 Fig. 12 shows the searched models in the NA process, taking $C25/C45$ in-
 398 version as an example. Because of the low sensitivity of Rayleigh wave V_{ph} with
 399 respect to V_p and ρ , many equivalent models are found, whereas the results of
 400 ΔV_s converge.

401 4.2. Robustness of ADTLSWI

402 In order to test the robustness of ADTLSWI approach, two-layer models with
 403 the presence of a structure perturbation are used with V_s variations in the deep
 404 layer (see Section 2.3 for more details). Spectral element Method simulates wave
 405 propagation in the two-layer medium as in the laboratory measurement, where
 406 the changes in the repeatline are considered only in the deep layer, with a vari-
 407 ation of V_s . Two repeatlines are tested with $V_{s_2} = 940\text{ m/s}$ and $V_{s_2} = 1038\text{ m/s}$
 408 respectively and other parameters and dimensions stay the same as the base-
 409 line. The dispersion curves (see Fig. B.5 in Appendix Appendix B) show that

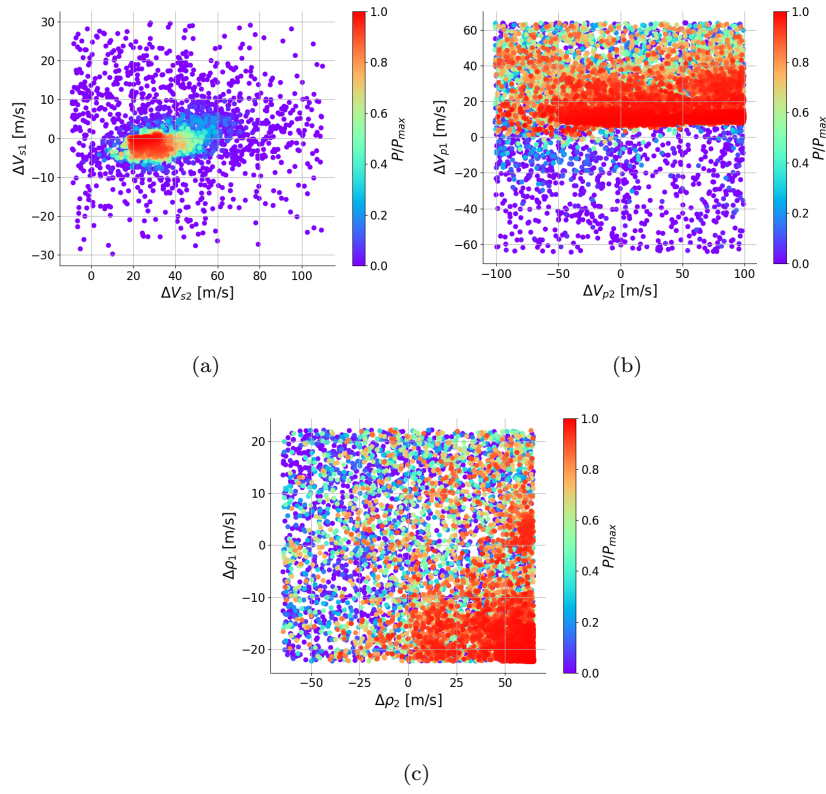


Figure 12: Searched model variations for ADTLSWI using *C25* as baseline and *C45* as repeatline.

baseline/repeatline	$\Delta V_{s_1}^{real}$	$\Delta V_{s_1}^{inv}$	$V_{s_1}^{real}$	$V_{s_1}^{inv}$
C25/C45	0	-0.2 (± 0.04)	708	707.8
C45/C65	0	-3.4 (± 0.06)	708	704.6

baseline/repeatline	$\Delta V_{s_2}^{real}$	$\Delta V_{s_2}^{inv}$	$V_{s_2}^{real}$	$V_{s_2}^{inv}$
C25/C45	20	21.2 (± 0.06)	1100	1101.2
C45/C65	60	54.3 (± 1.84)	1160	1154.3

Table 3: Comparison between the actual S-wave variations of the models and the inversion results by ADTLSWI. $V_{s_i}^{inv} = \Delta V_{s_i}^{inv} + V_{s_i}^{real}$ with $V_{s_i}^{real}$ the actual S-wave velocities of the epoxy-resin models. Unity: [m/s].

410 the cavity has less influence in models with $V_{s_2} = 1038 m/s$ which may due to
411 the higher wavelength. "Anomalies" created by cavity can be observed around
412 $50 kHz$ on the dispersion curves with $V_{s_2} = 940 m/s$ and $V_{s_2} = 990 m/s$, which
413 can be considered as "geological noise". Since the basic idea of differential in-
414 version is to use the difference caused by model variation and eliminate system
415 errors such as "geological noise", it makes sense to use models which are more
416 affected by cavity to test the robustness of ADTLSWI. Therefore, in the fol-
417 lowing, the model with $V_{s_2} = 940 m/s$ is used as the repeatline. Source and
418 receiver line are identical as in experimental test.

419 Dispersion curves are presented in Fig. 13 (a) in the frequency range $[40, 100] kHz$
420 and their difference ΔV_{ph} is presented in Fig. 13 (b). Dispersion curves are first
421 inverted separately using V_{ph} -SWI and then their subtraction is inverted using
422 ADTLSWI. Inversion results are presented in Table 4. V_{ph} -SWI and ADTLSWI

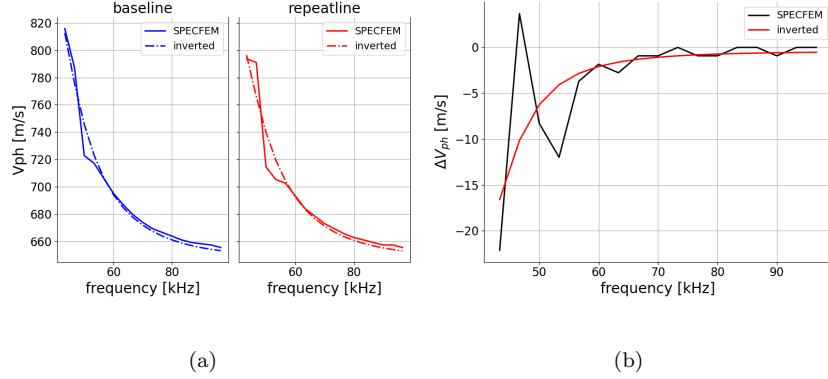


Figure 13: (a) Dispersion curves of simulated baseline and repeatline using SPEC2D software, and the corresponding calculated dispersion curve after applying V_{ph} -SWI. (b) Subtraction of two dispersion curves (repeatline minus baseline) and the calculated curve after ADTLSWI.

423 find $\Delta V_{s_2} = -47 \text{ m/s}$ and $\Delta V_{s_2} = -45 \text{ m/s}$ which gives 2.1% and 6.2% of error
 424 compared to real model variation.

425 5. Discussion

426 The inverted results in Table 3 for the epoxy-resin models confirms the
 427 adequation of ADTLSWI for the estimation of weak variations less than 5%. The

Table 4: Inversion results of dispersion curves using V_{ph} -SWI and ADTLSWI. V_p , ρ and h_1 are fixed during inversion. Parameter spaces for V_{ph} -SWI are $V_{s_1} \in [670, 730] \text{ m/s}$ and $V_{s_1} \in [900, 1130] \text{ m/s}$, and the ones for ADTLSWI are $\Delta V_{s_1} \in [-30, 30] \text{ m/s}$ and $\Delta V_{s_1} \in [-90, 90] \text{ m/s}$. Results are mean values for the 1000 models.

	true model	V_{ph} -SWI	ADTLSWI
$\Delta V_{s_1} [m/s]$	0	0	-0.5
$\Delta V_{s_2} [m/s]$	-48	-47	-45

428 inversion results of $C25/C45$ ($\alpha(V_{s_2}, C25, C45) = 1.8\%$) have smaller errors than
429 $C45/C65$ inversion ($\alpha(V_{s_2}, C45, C65) = 5.4\%$) thanks to its smaller variation
430 ratio. However, 5% of model variation cannot always be verified in the field
431 application. A preliminary study is required in this case to have an initial
432 understanding of the baseline and repeatline model variations. Besides, to use
433 the ADTLSWI approach, the baseline model must be well known since the
434 sensitivity kernel calculation is based on the baseline model parameters. The
435 PVD-SWI approach proposed by Wang et al. (2020b) can be applied to fulfill
436 these requirements thanks to the high sensitivity of the frequency derivative of
437 Rayleigh wave V_{ph} for both shallow and deep medium. From a practical point
438 of view, regular measurements are recommended to guarantee velocity variation
439 lower than 5% in field measurements. In the case of variations larger than
440 5%, some on-going works on non linearized differential time-lapse surface-wave
441 inversion (Wang et al., 2020a) should be more appropriate.

442 A prominent numerical advantage of the ADTLSWI is its short calculation
443 time as the sensitivity kernel is calculated only once based on the baseline model
444 parameters. However, this differential approach is accurately calculated for the
445 baseline model in the former numerical or experimental test, i.e. prior fine
446 inversion of the baseline data provide a robust reference model which avoids
447 the biases results on the repeatline by error propagation. Note that the study
448 presented here is based on a two-layer model for which only the fundamental
449 mode is suitable as it is dominant. In case of models including large contrasts
450 of parameters between layers, a study with multiple modes would be of interest.

451 In this case, the sensitivity kernel should be updated to contain the information
452 of multiple modes.

453 The small-scale models used here in order to apply the method make use of
454 ultrasonic techniques in a laboratory environment, which means that the exper-
455 iments are performed under controlled conditions with a fixed source position
456 and a shared generated source signal, controlled receiver positions with high
457 accuracy, which would be the case in a monitoring context where the sensors
458 are installed permanently, and well known epoxy-resin parameters. Questions
459 may be asked in the situation of field measurement, in the presence of unknown
460 structure under-surface, or in a more heterogeneous medium such as concrete.
461 The second robustness test using numerical data is performed under these con-
462 siderations by adding an heterogeneity that alters the dispersion curve.

463 Inversion results through ADTLSWI process are compared with the inversion
464 results of V_{ph} -SWI approach for models which contain a cavity. We demonstrate
465 that, with the same a priori information, ADTLSWI can be used to quickly
466 calculate model variations in case of wrongly calculated forward problem, even
467 if the results are slightly less accurate than those from V_{ph} -SWI. However, it is
468 undeniable that ADTLSWI is limited to small model variations (less than 5%)
469 and requires a relatively accurate baseline model.

470 A semi-global optimization approach, i.e. the Neighborhood Algorithm, is
471 applied for the linearized differential inversion. Attentions must be paid to differ-
472 entiate the differential inversion to the conventional linearized inverse problems,
473 because the Jacobian matrix for the former is $J(\Delta V_{ph}, \Delta \mathbf{m})$ and $J(V_{ph}, \mathbf{m})$ for

474 the latter. There is no associated error in the objective function in Eq. 4. The
475 classically applied errors in the surface-wave methods, e.g. the realistic error
476 in O'Neill (2004), are defined on the dispersion curve of V_{ph} , instead of ΔV_{ph} .
477 Therefore, it is not suitable to directly apply them in Eq. 4 for ADTLSWI. In
478 the case of field measurements, a possible way is to perform several shots for
479 baseline and repeatline recordings. The calculated standard deviation between
480 $\Delta V_{ph}^{i,j}(\mathbf{b}_i, \mathbf{r}_j)$ can be used as the data error in the inversion process.

481 **6. Conclusion**

482 An Analytical Differential Time-Lapse Surface-Wave Inversion (ADTLSWI)
483 is proposed in this study for the purpose of monitoring small variations of a
484 medium. It used the simple difference of two successive measured phase velocity
485 dispersion curves (ΔV_{ph}) as inversion input data. The latter were inverted
486 through the ADTLSWI by using a linear assumption of the Rayleigh wave phase
487 velocity and sensitivity kernels (which describe the partial derivative of the
488 Rayleigh wave phase velocity with respect to the model parameters) in order to
489 mathematically link ΔV_{ph} with variation of the model parameters $\Delta \mathbf{m}$.

490 The ADTLSWI approach was first tested on numerical data. Two-layer
491 models are used to simulate variations occurring in the shallow and deep layers.
492 The analysis of the process results showed that the linear approximation of the
493 Rayleigh wave phase velocity can be used when the variations are less than 5%.
494 The ADTLSWI method led to lower bias in the results of variations in the deep
495 layer than in the shallow layer. This behavior was due to the higher sensitivity

496 of the Rayleigh wave phase to variations of the S-waves in the shallow layer
497 than in the deep layer. Compared to the V_{ph} -SWI and PVD-SWI methods,
498 the ADTLSWI method is more efficient for estimating weak variations in media
499 (variations less than 5%), furthermore at a lower computational cost.

500 The ADTLSWI methodology was finally applied to laboratory data for ex-
501 perimental validation in the two-layer context, and to numerical data with a
502 structural perturbation (an under-surface cavity). The robustness of ADTL-
503 SWI is verified by these two tests. Indeed, the test with the laboratory data
504 was an intermediate step between numerical testing and field experiments. Even
505 numerical data generated by Spectral Element Method cannot simulate all com-
506 plex cases in real field measurement. Therefore, further studies with field data
507 and thus uncontrolled factors are the next steps.

508 **References**

509 Jonathan Ajo-Franklin, Shan Dou, Thomas Daley, Barry Freifeld, Michelle
510 Robertson, Craig Ulrich, Todd Wood, Ian Eckblaw, Nathan Lindsey, Eileen
511 Martin, et al. Time-lapse surface wave monitoring of permafrost thaw using
512 distributed acoustic sensing and a permanent automated seismic source. In
513 *SEG Technical Program Expanded Abstracts 2017*, pages 5223–5227. Society
514 of Exploration Geophysicists, 2017.

515 K Aki and P. G. Richards. *Quantitative Seismology, 2nd Ed.* University Science
516 Books, 2002.

517 Amir Asnaashari, Romain Brossier, Stéphane Garambois, François Audebert,

518 Pierre Thore, and Jean Virieux. Time-lapse imaging using regularized fwi: a
519 robustness study. In *SEG Technical Program Expanded Abstracts 2012*, pages
520 1–5. Society of Exploration Geophysicists, 2012.

521 Paolo Bergamo, Ben Dashwood, Sebastian Uhlemann, Russell Swift, Jonathan E
522 Chambers, David A Gunn, and Shane Donohue. Time-lapse monitoring of
523 climate effects on earthworks using surface waves. *Geophysics*, 81(2):EN1–
524 EN15, 2016.

525 François Bretaudeau, Donatienne Leparoux, Olivier Durand, and Odile Abra-
526 ham. Small-scale modeling of onshore seismic experiment: A tool to validate
527 numerical modeling and seismic imaging methods. *Geophysics*, 76(5):T101–
528 T112, 2011.

529 Marine Dangeard, L Bodet, S Pasquet, J Thiesson, R Guérin, D Jougnot, and
530 Laurent Longuevergne. Estimating picking errors in near-surface seismic data
531 to enable their time-lapse interpretation of hydrosystems. *Near Surface Geo-*
532 *physics*, 16(6):613–625, 2018.

533 Huseyin Denli and Lianjie Huang. Double-difference elastic waveform tomog-
534 raphy in the time domain. In *SEG Technical Program Expanded Abstracts*
535 *2009*, pages 2302–2306. Society of Exploration Geophysicists, 2009.

536 Adam M Dziewonski and Don L Anderson. Preliminary reference earth model.
537 *Physics of the earth and planetary interiors*, 25(4):297–356, 1981.

538 Céline Gélis, D Leparoux, Jean Virieux, Adnand Bitri, Stéphane Operto, and

539 Gilles Grandjean. Numerical modeling of surface waves over shallow cavities.
540 *Journal of Environmental & Engineering Geophysics*, 10(2):111–121, 2005.

541 Christophe Geuzaine and Jean-François Remacle. Gmsh: A 3-d finite element
542 mesh generator with built-in pre-and post-processing facilities. *International*
543 *journal for numerical methods in engineering*, 79(11):1309–1331, 2009.

544 Tatsunori Ikeda, Takeshi Tsuji, Mamoru Takanashi, Isao Kurosawa, Masashi
545 Nakatsukasa, Ayato Kato, Kyle Worth, Don White, and Brian Roberts. Tem-
546 poral variation of the shallow subsurface at the aquistore co2 storage site
547 associated with environmental influences using a continuous and controlled
548 seismic source. *Journal of Geophysical Research: Solid Earth*, 122(4):2859–
549 2872, 2017.

550 Anaëlle Joubert, Mathieu Le Feuvre, and Philippe Côte. Passive monitoring
551 of a sea dike during a tidal cycle using sea waves as a seismic noise source.
552 *Geophysical Journal International*, 214(2):1364–1378, 2018.

553 Dimitri Komatitsch and Jeroen Tromp. Introduction to the spectral element
554 method for three-dimensional seismic wave propagation. *Geophysical journal*
555 *international*, 139(3):806–822, 1999.

556 Dimitri Komatitsch and Jean-Pierre Vilotte. The spectral element method:
557 an efficient tool to simulate the seismic response of 2d and 3d geological
558 structures. *Bulletin of the seismological society of America*, 88(2):368–392,
559 1998.

560 Zhiqu Lu. Feasibility of using a seismic surface wave method to study seasonal
561 and weather effects on shallow surface soils. *Journal of Environmental and*
562 *Engineering Geophysics*, 19(2):71–85, 2014.

563 William Menke. *Geophysical data analysis: Discrete inverse theory*. Academic
564 press, 2018.

565 Talal A Mokhtar, RB Herrmann, and DR Russell. Seismic velocity and q model
566 for the shallow structure of the arabian shield from short-period rayleigh
567 waves. *Geophysics*, 53(11):1379–1387, 1988.

568 Aurélien Mordret, Roméo Courbis, Florent Brenguier, Małgorzata Chmiel,
569 Stéphane Garambois, Shujuan Mao, Pierre Boué, Xander Campman, Thomas
570 Lecocq, Wim Van der Veen, et al. Noise-based ballistic wave passive seismic
571 monitoring—part 2: surface waves. *Geophysical Journal International*, 221(1):
572 692–705, 2020.

573 Adam O’Neill. Shear velocity model appraisal in shallow surface wave inver-
574 sion. In *Symposium on the Application of Geophysics to Engineering and*
575 *Environmental Problems 2004*, pages 1544–1555. Society of Exploration Geo-
576 physicists, 2004.

577 D Pageot, D Leparoux, O Durand, M Le Feuvre, P Côte, and Y Capdeville.
578 Refined experimental studies for improving the reduced-scale physical model-
579 ing of seismic subsurface measurement. In *Near Surface Geoscience 2015-21st*
580 *European Meeting of Environmental and Engineering Geophysics*, 2015.

- 581 Damien Pageot, Donatienne Leparoux, Mathieu Le Feuvre, Olivier Durand,
582 Philippe Côte, and Yann Capdeville. Improving the seismic small-scale mod-
583 elling by comparison with numerical methods. *Geophysical Journal Interna-*
584 *tional*, 211(1):637–649, 2017.
- 585 Choon Byong Park, Richard D. Miller, and Jianghai Xia. Imaging dispersion
586 curves of surface waves on multi-channel record. *SEG Expanded Abstracts*, 17
587 (1):1377–1380, 1998. ISSN 10523812. doi: 10.1190/1.1820161.
- 588 Sylvain Pasquet, Ludovic Bodet, Amine Dhemaied, Amer Mouhri, Quentin Vi-
589 tale, Fayçal Rejiba, Nicolas Flipo, and Roger Guérin. Detecting different
590 water table levels in a shallow aquifer with combined p-, surface and sh-wave
591 surveys: Insights from vp/vs or poisson’s ratios. *Journal of Applied Geo-*
592 *physics*, 113:38–50, 2015.
- 593 T. Planès, M. A. Mooney, J. B. R. Rittgers, M. L. Parekh, M. Behm, and
594 R. Snieder. Time-lapse monitoring of internal erosion in earthen dams and
595 levees using ambient seismic noise. *Géotechnique*, 66(4):301–312, 2016. ISSN
596 0016-8505. doi: 10.1680/jgeot.14.P.268.
- 597 Malcolm Sambridge. Geophysical inversion with a neighbourhood algorithm—ii.
598 appraising the ensemble. *Geophysical Journal International*, 138(3):727–746,
599 1999a.
- 600 Malcolm Sambridge. Geophysical inversion with a neighbourhood algorithm—i.
601 searching a parameter space. *Geophysical journal international*, 138(2):479–
602 494, 1999b.

- 603 H Takeuchi, M Saito, and BA Bolt. Seismic surface waves. *Methods in compu-*
604 *tational physics*, 11:217–295, 1972.
- 605 Albert Tarantola. *Inverse problem theory and methods for model parameter*
606 *estimation*, volume 89. siam, 2005.
- 607 Raphaël Valensi, Donatienne Leparoux, Olivier Durand, François Bretaudeau,
608 and Philippe Côte. Multicomponent reduced scale seismic modelling: up-
609 grade of the musc laboratory with application to polarization observations.
610 *Geophysical Journal International*, 202(3):1993–2024, 2015.
- 611 A Wang, D Leparoux, and O Abraham. Differential inversion of surface wave
612 methods: Proposition of diagram distance as inversion data. In *26th European*
613 *Meeting of Environmental and Engineering Geophysics*, 2020a.
- 614 A Wang, D Leparoux, O Abraham, and M Le Feuvre. Frequency derivative
615 of rayleigh wave phase velocity for fundamental mode dispersion inversion:
616 parametric study and experimental application. *Geophysical Journal Inter-*
617 *national*, 2020b.
- 618 Toshiki Watanabe, Shoshiro Shimizu, Eiichi Asakawa, and Toshifumi Matsuoka.
619 Differential waveform tomography for time-lapse crosswell seismic data with
620 application to gas hydrate production monitoring. In *SEG Technical Program*
621 *Expanded Abstracts 2004*, pages 2323–2326. Society of Exploration Geophysi-
622 cists, 2004.
- 623 Wathelet. Surface-wave inversion using a direct search algorithm and its appli-

- 624 cation to ambient vibration measurements. *Near Surface Geophysics*, pages
625 211–221, 2004. doi: 10.3997/1873-0604.2004018.
- 626 Marc Wathelet. An improved neighborhood algorithm: parameter conditions
627 and dynamic scaling. *Geophysical Research Letters*, 35(9), 2008.
- 628 Di Yang, Mark Meadows, Phil Inderwiesen, Jorge Landa, Alison Malcolm, and
629 Michael Fehler. Double-difference waveform inversion: Feasibility and robust-
630 ness study with pressure data. *Geophysics*, 80(6):M129–M141, 2015.

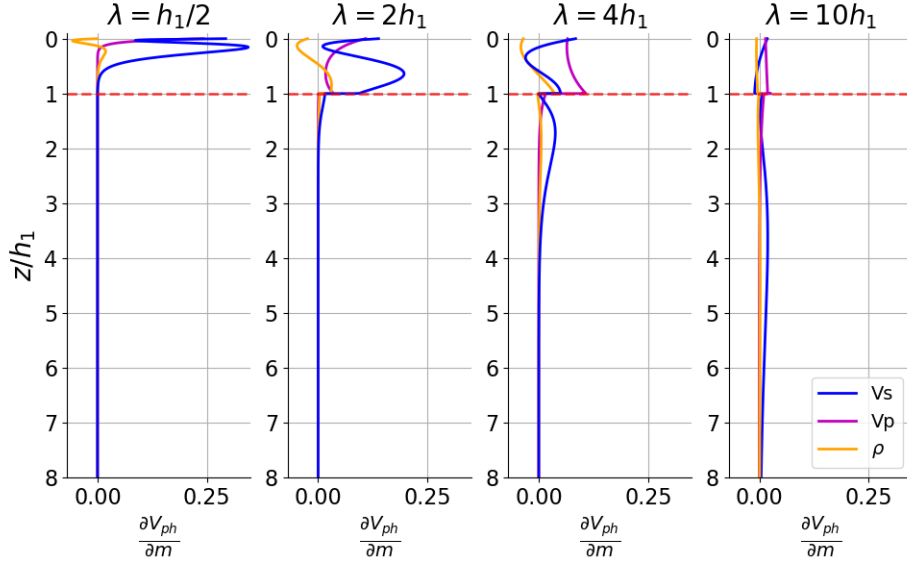


Figure A.1: Sensitivity curves of the Rayleigh wave phase velocity of a two-layer model (parameters available in Table 1) at four different wavelengths (or frequencies), presented as a function of normalized depth. h_1 is the first layer thickness.

631 Appendix A. Sensitivity kernel of Rayleigh wave phase velocity

632 Fig. A.1 shows the sensitivity curves of the Rayleigh phase velocity with
 633 respect to model parameters V_s , V_p and ρ , as a function of depth. Sensitivity
 634 curves are calculated at four wavelengths (frequencies): $\lambda = \frac{h_1}{2}$, $\lambda = 2h_1$,
 635 $\lambda = 4h_1$ and $\lambda = 10h_1$. It can be observed that V_{ph} is more sensitive to the
 636 variation of the V_s than to variations of V_p and ρ , especially at depth (i.e. below
 637 the first layer thickness h_1), since the values of the sensitivity with respect to
 638 V_p and ρ are almost zero below this depth. Model parameters are available in
 639 Table 1.

640 The sensitivity kernel of V_{ph} with respect to model parameter of each layer is

641 calculated numerically using the model parameters in Table 1 and presented in
642 Fig. A.2. The maximum depth for the integration calculation is equal to $10h_1$.
643 Fig. A.2 shows that V_s has more effect on the Rayleigh wave V_{ph} , especially for
644 greater depths. Indeed, the maximum ratio of the sensitivity kernels of V_s to
645 V_p and ρ is higher for the deep layer.

646 **Appendix B. Simulated data using SPECFEM2D**

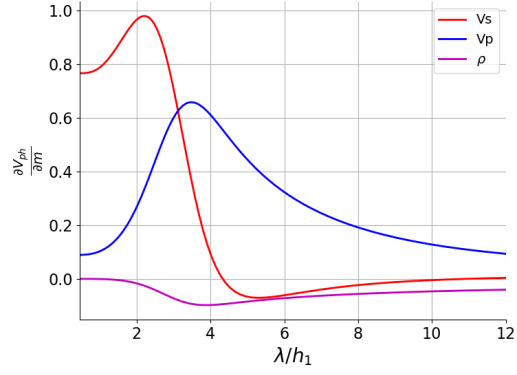
647 Geometry of model is available in Table 2. Settings and parameters for
648 numerical calculation by SPECFEM2D (Komatitsch and Vilotte, 1998; Ko-
649 matitsch and Tromp, 1999) and the mesh is generated by Gmsh (Geuzaine
650 and Remacle, 2009):

- 651 - Maximum and minimum grid size [mm]: 1.6, 0.5
- 652 - Average and minimum GLL point distance [mm]: 0.13, 0.09
- 653 - Time step [ms]: 2×10^{-5} .

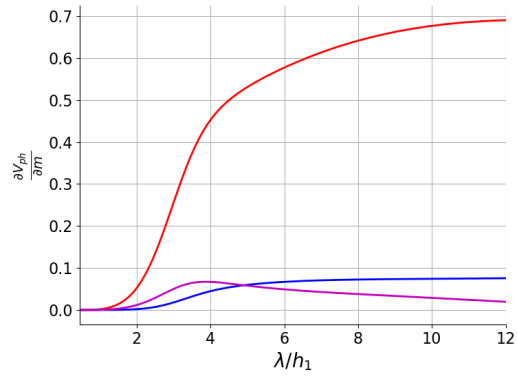
Declaration of interests

The authors declare that they have no known competing financial interests or personal relationships that could have appeared to influence the work reported in this paper.

The authors declare the following financial interests/personal relationships which may be considered as potential competing interests:



(a)



(b)

Figure A.2: Rayleigh wave phase velocity sensitivity kernel with respect to model parameters V_p , V_s and ρ of (a) the shallow layer (layer 1 of Table 1) and (b) deep layer (layer 2 of Table 1), as a function of the wavelength divided by the thickness of the shallow layer h_1 .

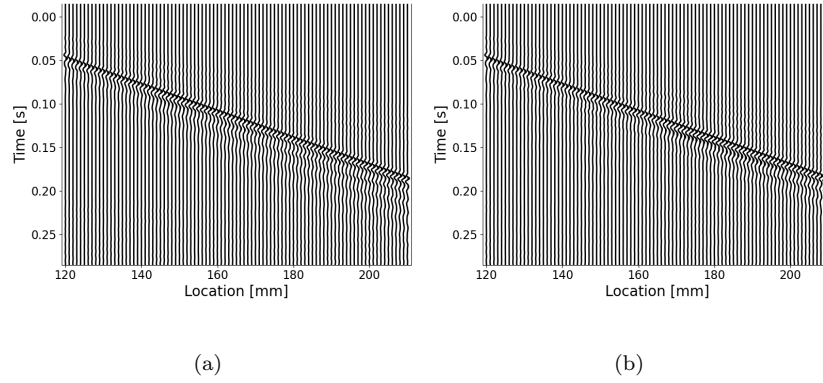


Figure B.3: Seismograms of numerical models (a) without cavity and (b) with cavity.

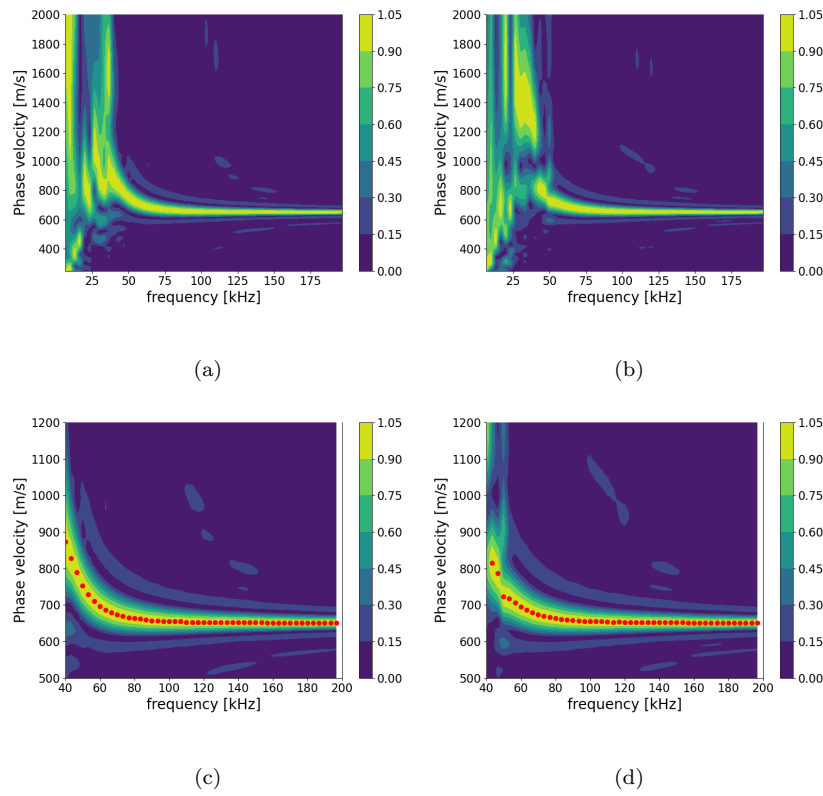


Figure B.4: Dispersion diagrams of numerical models (a) without cavity and (b) with cavity and the pickings of dispersion curves in (c) and (d).

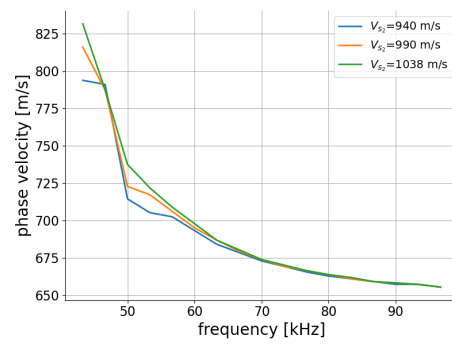


Figure B.5: Dispersion curves of numerical models with cavity.